Discover Applied Sciences

Research

Load specific phase-field based structural optimization and experimental validation of sheet-based gyroid structures

Leonie Wallat[1,2,3] · Michael Selzer[1,4] · Marcus Seiler[5] · Frank Poehler[2] · Britta Nestler[1,3,4]

Received: 23 December 2024 / Accepted: 25 May 2025

Abstract
In the following, a detailed investigation of two phase-field based variants for optimizing unidirectionally loaded gyroid unit cells is presented. The optimization is conducted within the linear-elastic range, aiming to maximize the stiffness of the structure while preserving its periodicity. In the first approach, a gyroid unit cell with an initial porosity of approximately 75% is volumetrically reduced by 5%. This volume reduction in the less stressed regions results in a topological modification of the structure. In the second approach, a gyroid unit cell with an initial porosity of approximately 80% is also volumetrically reduced by 5%. Subsequently, the volume is increased by 5% through a phase-field based shape optimization process, resulting in a final porosity of 80%. Both modified structures are compared to a reference structure-an unmodified gyroid structure with a porosity of 80%. The results indicate that the modified structures exhibit an approximately 32% higher effective Young's modulus. Furthermore, a correlation between the simulation results and experimental data is established.

Keywords Topology modification · Shape optimization · Gyroid · TPMS-structures · Phase-field

1 Introduction

Cellular structures are found in various forms in nature, with the honeycomb being a well-known example [1, 2]. These structures are often characterized by their high strength combined with low weight, making them highly attractive for a wide range of applications, including aerospace, medical engineering, and energy absorption systems [3, 4]. For example, in [4], spider web lattice structures were used to develop vibration dampers in small electric aircraft motors. Advances in additive manufacturing technologies, particularly electron beam melting, fused deposition modeling (FDM), and stereolithography (SL), now enable the fabrication of far more complex structures that were previously unattainable with conventional manufacturing methods. One example of such structures is triply periodic minimal surfaces (TPMS), which are distinguished by their smooth, curved surfaces and periodicity in all spatial directions [5]. As an example, Fig. 1 illustrates a TPMS unit cell of the sheet-based gyroid structure with a porosity of 80%. These cellular structures can be generated through a mathematical approximation [6, 7].

✉ Leonie Wallat, leonie.wallat@partner.kit.edu; ✉ Michael Selzer, michael.selzer@kit.edu | [1]Institute of Digital Materials Science, Karlsruhe University of Applied Sciences, Moltkestraße 30, 76133 Karlsruhe, Baden-Wuerttemberg, Germany. [2]Institute of Materials and Processes, Karlsruhe University of Applied Sciences, Moltkestraße 30, 76133 Karlsruhe, Baden-Wuerttemberg, Germany. [3]Institute for Applied Materials - Microstructure Modelling and Simulation, Karlsruhe Institute of Technology (KIT), Strasse am Forum 7, 76131 Karlsruhe, Baden-Wuerttemberg, Germany. [4]Institute of Nanotechnology, Karlsruhe Institute of Technology (KIT), Hermann-von-Helmholtz-Platz 1, 76344 Eggenstein-Leopoldshafe, Baden-Wuerttemberg, Germany. [5]ReOss GmbH, Echterdinger Str. 57, 70794 Filderstadt, Baden-Wuerttemberg, Germany.

Discover Applied Sciences (2025) 7:742 | https://doi.org/10.1007/s42452-025-07204-w

The potential applications for these structures are diverse, ranging from tissue-engineering [8] to crash structures [9]. In many studies, the focus is on mechanical properties. For example, mechanical stability is crucial in the use of bone scaffolds, where sufficient stability must be provided to support the scaffold while matching the mechanical properties of the surrounding bone to avoid stress shielding [10, 11]. In [8], three different TPMS microarchitectures (Diamond, Gyroid, and Primitive) were investigated as potential scaffolds for bone tissue engineering in regenerative medicine. The results showed that the Diamond and Gyroid structures exhibited higher compressive strength compared to the Primitive structure. This observation has been corroborated by other studies, which found that the Primitive structure demonstrated the lowest strength, followed by the Gyroid, with the Diamond structure showing the highest strength [12]. Furthermore, the Diamond- and Gyroid-based scaffolds exhibited the highest bone growth and bone-to-implant contact in vivo.

Al-Ketan [13] investigated the mechanical properties of both sheet- and strut-based TPMS structures and demonstrated that sheet-based structures exhibit superior mechanical properties regardless of their porosity.

Due to the wide range of research and application areas for TPMS structures and the possibility of fabricating arbitrary geometrical structures by additive manufacturing, various optimization approaches have been developed to further improve specific properties of these structures. As the review paper [14] illustrates, most optimization approaches aim at improving effective mechanical properties like stiffness or yield strength. For example, in [15], the mechanical properties of a heat exchanger for the aerospace industry were optimized. This was achieved by adjusting parameters such as cell size, wall thickness, and periodic length. Most optimization methods are based on shape optimization, which, unlike topology optimization, does not alter the initial topology of the structure [16].

One approach for shape optimization involves the introduction of porosity or cell gradients [17–19]. These gradients, for example, vary the porosity within the structure, which can lead to changes in the heat transfer coefficient, drag resistance [19], or effective stiffness [17].

Another popular optimization method which can be found in the literature is the density-based solid isotropic material with penalization (SIMP) approach [20–22], which can also be applied to TPMS cells. For example, TPMS lattice structures were shape optimized for different loading conditions in [22] using the SIMP-approach.

A less explored optimization approach for complex porous structures is based on the phase-field method. A key advantage of this method is its ability to accommodate complex geometrical changes without the need to adjust the numerical discretization [23], enabling the generation of novel, organic structures that can better meet functional requirements than conventional designs [24]. This distinguishes PFM based methods from others like the SIMP approach, where geometry-fitted meshes are required. Optimization methods based on introducing porosity gradients limits the degree of freedom for geometry adjustment to the gradient distribution function. While this leads to high computation efficiency, it limits the optimization potential compared to PFM-based optimization, where the complete mass distribution in the domain, by means of the phase-field, can freely vary. Furthermore, gradient-based methods tend to disrupt characteristic properties such as the periodicity of the structure [17]. In contrast, by applying appropriate boundary conditions in the phase-field method, it is possible to optimize a single unit cell while preserving its periodicity. This allows the optimized structure to be repeated in all spatial directions and adapted to the specific application.

In [25], unit-cell TPMS structures (Diamond, Primitive, and Gyroid) were shape optimized using the phase-field method under uniaxial loading, with volume preservation. While this optimization led to an increase in the effective elastic modulus, it also disrupted the periodicity, one of the characteristic features of these structures. Subsequent experimental

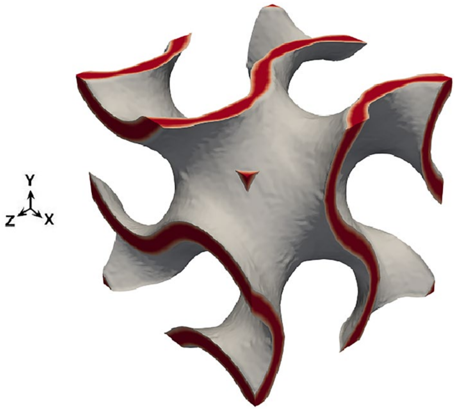

Fig. 1 Sheet-based gyroid unit-cell with a porosity of 80%

validations revealed a correlation between simulation and experimental data [12]. In another publication [26], sheet-based Gyroid structures with varying porosities (75%, 80%, and 85%) were shape optimized under uniaxial and multi-axial loading while maintaining their periodicity. The experimental validation of the uniaxially optimized structures also showed good agreement with the simulation results.

While these previous works already show the feasibility of PFM-based optimization to improve TPMS structures, they are limited to shape optimization without topological changes. PFM-based topology optimization is also possible, but so far mainly focuses on two-dimensional setups [27–29]. The novelty of the present work lies in extending the optimization of three-dimensional TPMS-structures by combining topology and shape optimization. The optimization is applied on a gyroid structure and aims at increasing the stiffness while preserving its periodicity. Two different PFM-based approaches for combined topology and shape optimization are introduced, applied, and compared. Furthermore, the initial gyroid structure and the resulting optimized structures are fabricated using additive manufacturing and experimentally tested under mechanical load to confirm the improvements.

Two different optimization approaches are pursued: In the first approach, a gyroid structure with an initial volume of 25%, corresponding to a porosity of 75%, is examined. Through a load-specific volume reduction, the volume is decreased by 5%, leading to a topological modification of the structure.

In the second approach, a gyroid structure with an initial porosity of 80% is also reduced by approximately 5%. Subsequently, this structure undergoes shape optimization using a phase-field based approach. Since no volume-preserving method was applied, the volume increases during the optimization process. Once the original porosity of 80% is reached again, the optimization loop is stopped. As a comparison for these two modified structures, an unaltered sheet-based gyroid structure with a porosity of 80% is used. In addition to simulation-based evaluations, the structures are also experimentally validated.

1.1 Approach and method

In this section, the two different optimization approaches applied in the present work are introduced.

In the first approach, a sheet-based gyroid structure with an initial porosity of 75% is topologically modified under unidirectional loading in the linear-elastic range through the hole nucleation process, as described in the following chapter 1.1.2. This modification is load-specific, resulting in a final porosity of 80%.

In the second method, the comparison structure with a porosity of 80% is directly reduced in volume by approximately 5% through the topology modification process under unidirectional loading. Subsequently, a phase-field based shape optimization is carried out while maintaining the periodicity of the structure. Since no volume-preserving approach is applied during the shape optimization process, the volume increases. The optimization is terminated once the initial volume of the structure is restored. For the mathematical derivation of the phase-field based shape optimization, please refer to [26]. These two approaches to load-specific structural modification are summarized in Fig. 2.

Subsequently, experimental validation is conducted. The fabrication of the structures, testing, and evaluation are orientated according to the ASTM D1621 standard.

1.1.1 Simulation and used software

For the simulations conducted and the creation of the gyroid unit cell, the in-house simulation software "Parallel Algorithms for Crystal Evolution in 3D" (Pace3D) is used [30]. This tool allows the generation of other TPMS structures and the integration of features such as porosity gradients, furthermore, it supports structural-mechanical simulations based on the phase-field approach for various loading scenarios.

For the topological modification and optimization, a modified phase-field approach is employed, which is based on the Allen-Cahn method [31]. The evolution of the phase-field is derived from the minimization of a Ginzburg-Landau free energy density functional, which depends on the phase-field tuple and the corresponding gradients [32]. Subsequently, the mathematical model formulation for phase-field based shape optimization is briefly introduced. For more details, it is referred to [12] and [26], where the same shape optimization approach is employed.

Objective function The structures examined in this study are specifically optimized with respect to their effective stiffness to enhance their mechanical performance under the given uni-axial loading. As demonstrated in previous studies [12, 26], two different kind of boundary conditions can be applied prescribing either effective stress $\bar{\boldsymbol{\sigma}}$ or effective strain $\bar{\boldsymbol{\varepsilon}}$. As objective function, the strain energy density $\bar{f}_{\mathrm{el}}$ is considered which is calculated as

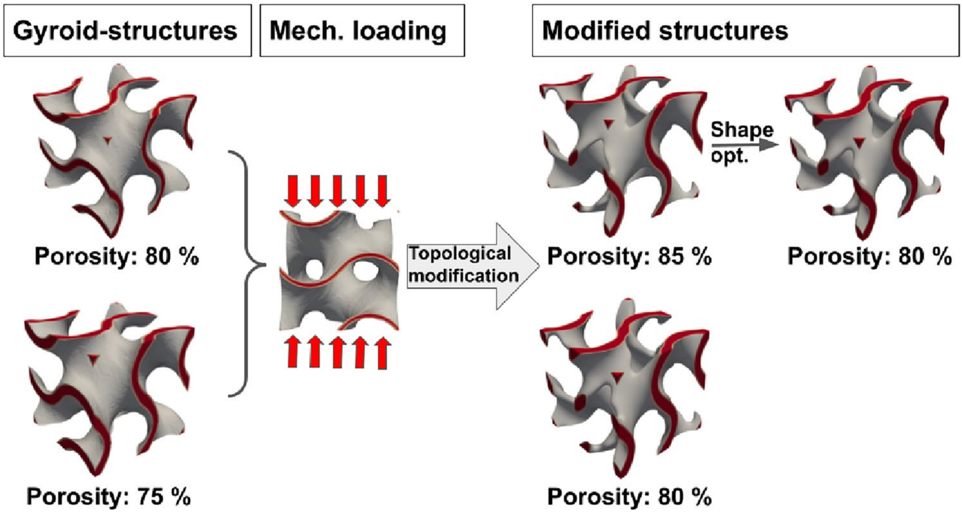

Fig. 2 Illustration of the two load-specific structural modification approaches: 1. Topological modification of a gyroid structure with an initial porosity of 75%; 2. Topological modification followed by shape optimization of a gyroid structure with an initial porosity of 80%

$$\bar{f}_{\mathrm{el}} = \bar{f}^{*}_{\mathrm{el}} = \frac{1}{2}\bar{\boldsymbol{\sigma}} \cdot \bar{\mathbb{S}}[\bar{\boldsymbol{\sigma}}] = \frac{1}{2}\bar{\boldsymbol{\epsilon}} \cdot \bar{\mathbb{C}}[\bar{\boldsymbol{\epsilon}}] \tag{1}$$

for a linear elastic material with the effective stiffness and compliance tensors $\bar{\mathbb{C}}$, and $\bar{\mathbb{S}}$, respectively. In the first case of prescribing the effective stress $\bar{\boldsymbol{\sigma}}$, an increase in the effective stiffness is achieved by minimizing the strain energy $\min(\bar{f}_{\mathrm{el}})$ as the structure is designed to undergo minimal deformation under a given load. In case of a prescribed effective strain $\bar{\boldsymbol{\epsilon}}$, increasing the effective stiffness corresponds to maximizing the strain energy. In the present study, the first case of a prescribed effective stress is considered.

Phase-field evolution equation and model parameters The phase-field evolution equation can be derived based on the Allen-Cahn approach in order minimize a free energy functional comprising interfacial and the strain energy density as bulk term. In the present work, an obstacle potential as well as a correction term that eliminates the curvature-minimizing dynamics of the Allen-Cahn equation is employed. For the gyroid structure, where the volume is preserved during optimization, an additional volume-conserving parameter is considered. For a more detailed mathematical derivation, we refer to [12] and [26].

Accordingly, the set of partial differential equations considered in the optimization process are the stationary momentum and Allen-Cahn equation given by

$$\nabla \cdot (\boldsymbol{\sigma}) = 0, \tag{2}$$

$$\frac{\partial \phi_{\mathrm{s}}}{\partial t} = \frac{M}{\epsilon}\left[2\gamma\epsilon(\Delta\phi_{\mathrm{s}} - \|\nabla\phi_{\mathrm{s}}\|\nabla\cdot\boldsymbol{n}) - \frac{16\gamma}{\pi^2\epsilon}(< spanclass =' convertEndash' > 1 - 2 < /span > \phi_{\mathrm{s}}) - \lambda_{\mathrm{vol}} + \frac{\partial h(\phi_{\mathrm{s}})}{\partial\phi_{\mathrm{s}}}\bar{f}_{\mathrm{el}}\right]. \tag{3}$$

Here, M denotes the mobility coefficient, γ represents the surface tension, and ϵ is a parameter that determines the width of the diffuse interface employed within the phase-field method. Volume preservation is ensured by the Lagrange multiplier λ_{vol} (cf. [33]). Furthermore, the term $|\nabla\phi_{\mathrm{s}}|\nabla\cdot\boldsymbol{n}$ with $\boldsymbol{n} := \nabla\phi_{\mathrm{s}}/|\nabla\phi_{\mathrm{s}}|$ eliminates the curvature-minimizing dynamics of the Allen-Cahn equation (3) (see [34, 35]). As a result, the interface terms proportional to γ only contribute to a relaxation towards the phase-field equilibrium profile, while preserving the actual geometry, which can be identified by the iso-surface at $\phi_{\mathrm{s}} = 0.5$.

The gyroidal unit cells considered in this work are embedded in a three-dimensional domain Ω, which contains 200cells in each spatial direction. For the structural optimization, the following parameters are employed to solve the differential equation 3: The parameter $\epsilon = 0.015L$ is chosen. This corresponds to an interface width of approximately $0.0375L$ within a domain of edge length $L = 1$ m. Additionally, the diffuse interface is resolved using 7 cells. Furthermore, a mobility parameter of $M = 1.0\,\mathrm{m}^2\,\mathrm{s}\,\mathrm{kg}^{-1}$ and a time step size of $\Delta t = 1.75 \times 10^4$ s and a surface tension of $\gamma = 0.02\,\mathrm{kg}\,\mathrm{s}^{-2}$ are specified. To solve the system of differential equations, the software package Pace3D [30] is used, a software framework for simulating microstructure evolution based on the phase-field method. The phase-field evolution equation (3) is discretized using a finite-difference method with explicit time-step integration on a Cartesian grid. In each time step, the stationary momentum balance (2) is solved using a linear finite element discretization. Further details on the solution procedure and coupling of the phase-field equation with the momentum balance may be found in [12] and [36].

Boundary condition A two-phase problem is considered, with a solid phase (ϕ_{s}) and a porous phase (ϕ_{p}), which exhibits no stiffness. For the mechanical analysis, an average stress $\bar{\boldsymbol{\sigma}}$ is used, which, in addition to periodicity, must satisfy the following condition:

$$\bar{\boldsymbol{\sigma}} = \frac{1}{\Omega}\int_{\Omega} \sigma\big(\phi_{\text{s}}, \boldsymbol{u}(\phi_{\text{s}})\big)\, \mathrm{d}V, \tag{4}$$

where $\bar{\boldsymbol{\sigma}}$ denotes the average stress, ϕ_s is the solid phase and $\boldsymbol{u}$ corresponds to the displacement field in a three-dimensional domain Ω.

The approach consists of generating the average stress by selecting the average strain through displacement boundary conditions in an iterative procedure, so that the elastic free energy contribution $\tilde{\mathcal{F}}_{\text{el}}$ is chosen as the driving force:

$$\tilde{\mathcal{F}}_{\text{el}}(\phi_{\text{s}}, \tilde{\boldsymbol{u}}(\phi_{\text{s}}), \bar{\epsilon}(\phi_{\text{s}})) = \int_{\Omega} \frac{1}{2}\mathbb{C}(\phi_{\text{s}})[\epsilon(\tilde{\boldsymbol{u}}(\phi_{\text{s}})) + \bar{\epsilon}(\phi_{\text{s}})] \cdot \left[\epsilon(\tilde{\boldsymbol{u}}(\phi_{\text{s}})) + \bar{\epsilon}(\phi_{\text{s}})\right]\, \mathrm{d}V, \tag{5}$$

with the fourth order stiffness tensor $\mathbb{C}$. Furthermore, $\tilde{\boldsymbol{u}}$ and $\bar{\epsilon}$ decomposed the displacement field $\boldsymbol{u}$. This introduces an additional dependency of the functional on $\bar{\epsilon}$ with respect to ϕ_s, i.e., $\tilde{\mathcal{F}}_{\text{el}}(\phi_{\text{s}}, \tilde{\boldsymbol{u}}(\phi_s), \bar{\epsilon}(\phi_s))$. Accordingly, for a given strain $\epsilon^{(n)}$ in the iteration step n, the elastic equilibrium is solved and then updated for the next iteration step $(n+1)$.

$$\bar{\boldsymbol{\epsilon}}^{(n+1)} = \bar{\boldsymbol{\epsilon}}^{(n)} + \bar{\mathbb{C}}^{-1}(\phi_{\text{s}}) \cdot \left(\bar{\boldsymbol{\sigma}} - \frac{1}{\Omega}\int_{\Omega} \boldsymbol{\sigma}(\phi_{\text{s}}, \boldsymbol{u}^{(n+1)})\, \mathrm{d}V\right) \tag{6}$$

with the fourth order averaged stiffness tensor $\bar{\mathbb{C}} = \int \mathbb{C}_s \phi_s dV$. The initial strain $\epsilon^{(0)} = (\bar{\mathbb{C}}(\phi_s))^{-1}\bar{\boldsymbol{\sigma}}$ is used.

To obtain the macroscopic elastic behavior of a structure under a specific loading, a homogenization method is required to determine effective properties using the field information from the full-field simulation. From the obtained field information $\bar{\boldsymbol{\sigma}}$ and $\bar{\epsilon}$, the effective Young's modulus can be determined according to the approach from [37].

In the following, a stress of $\sigma = -7$ is applied in unidirectional loading in y–direction.

$$\bar{\sigma}_{\text{loadCase}} = \begin{bmatrix} 0 & -\sigma & 0 \\ -\sigma & 0 & 0 \\ 0 & 0 & 0 \end{bmatrix} \tag{7}$$

For topology modification, material is removed from the structure in less stressed areas according to the considered loading criteria. The process of volume reduction is described as *Hole Nucleation* in Chapter 1.1.2.

Comparison of Simulation and Experimental Data All simulations are conducted using a small deformation framework with a linear elastic material law. Therefore, due to the linearity, the simulation results independent of the stiffness of the solid material the structures are made of. Following [37], the subsequent simulation results are presented in a normalized form, where the effective elastic modulus is normalized by the elastic modulus of the solid material E_s. A comparison of the simulation and experimental data confirms a similar increase in the stiffness of the optimized structures.

1.1.2 Hole nucleation

The Hole Nucleation process is used for a stress-specific volume reduction based on the von Mises stress, σ_{vM}. By specifying a certain percentage value ρ_{Nuc}, material is removed from less stressed regions, resulting in a topological modification.

For the initial determination of the von Mises stress across the simulation domain, the considered gyroid unit cell is discretized using a Cartesian grid. Simulations are then performed until mechanical equilibrium under the given loading conditions is reached. The maximum value of the von Mises stress, $\max(\sigma_{\text{vM}})$, together with the previously defined percentage value (ρ_{Nuc}), serves as the threshold for nucleation. The hole nucleation occurs when following equation is satisfied:

$$\sigma_{\text{vM}} < \rho_{\text{Nuc}} \max(\sigma_{\text{vM}}) \tag{8}$$

In the cells of the computational grid where the von Mises stress falls below the threshold $\rho_{\text{Nuc}} \max(\sigma_{\text{vM}})$, a hard phase assignment is applied. Values initially assigned to the porous phase, $\phi_{\text{p}} = 0$, are now given the phase field value $\phi_{\text{s}} = 1$. This results in a stress-specific volume reduction, accompanied by a topological modification.

The percentage value ρ_{Nuc} for each of the considered gyroid structures is determined individually, ensuring that the resulting structure undergoes an approximate volume reduction of 5%.

2 Results and discussion

Two gyroidal, topologically modified unit cells with a porosity of approximately 80%, as shown in Fig. 2, are compared both numerically and experimentally with an initial gyroid structure, which also has a porosity of around 80%. All three structures are subjected to a stress in $y-$direction.

2.1 Topology modified and optimized structures

The gyroidal modified unit cells differ in their creation process. The first structure, referred to as $Gyroid75_{Nuc}$ (Fig. 3(a)), is based on a gyroidal unit cell with an initial porosity of approximately 75%. Through the previously described hole nucleation process, the volume is reduced by 5% under unidirectional loading in the *y*-direction, resulting in a final porosity of 80% after the modification. The second modified unit cell, $Gyroid80_{NucShape}$ (Fig. 3(b)), originates from a gyroidal reference structure with an initial porosity of approximately 80%. Similar to the first structure, the volume is initially reduced by 5% through the hole nucleation process. Subsequently, the volume-reduced structure undergoes shape optimization under load in the *y*-direction. Since no volume-preserving method is applied during this shape optimization, the process leads to an increase in volume. The optimization is concluded once the initial porosity of around 80% is restored.

Fig. 3 represents the two resulting modified structures.

Although two different topology-modification approaches were used, both structures exhibit remarkable similarities in the final outcome. Since the differences between the modified gyroid structures are barely noticeable, the volume fraction along the *x*-axis is plotted for a clearer representation of the structural modifications. Figure 4 compares the $Gyroid75_{Nuc}$ and $Gyroid80_{NucShape}$ structures with the unmodified gyroid unit cell.

In the diagram, the solid black line represents the gyroid unit cell with a porosity of 80%, while the blue dashed line corresponds to the $Gyroid75_{Nuc}$ structure, and the green dotted line represents the $Gyroid80_{NucShape}$ structure. Upon analyzing the topologically modified structures, it becomes evident that the volume reduction in both structures primarily occurs in the layers positioned along the *x*-axis at approximately 50 and 150, which correspond to the locations of the crossbars. This reduction in the crossbars is clearly observed in Fig. 3. For better visualization, the areas where material was removed from the initial gyroid unit cell are highlighted in Fig. 5.

Additionally, the volume distribution in Fig. 3 shows that the vertical columns, loaded in the *y*-direction, remain intact in the $Gyroid75_{Nuc}$ structure and are reinforced in the $Gyroid80_{NucShape}$ structure during the shape optimization process.

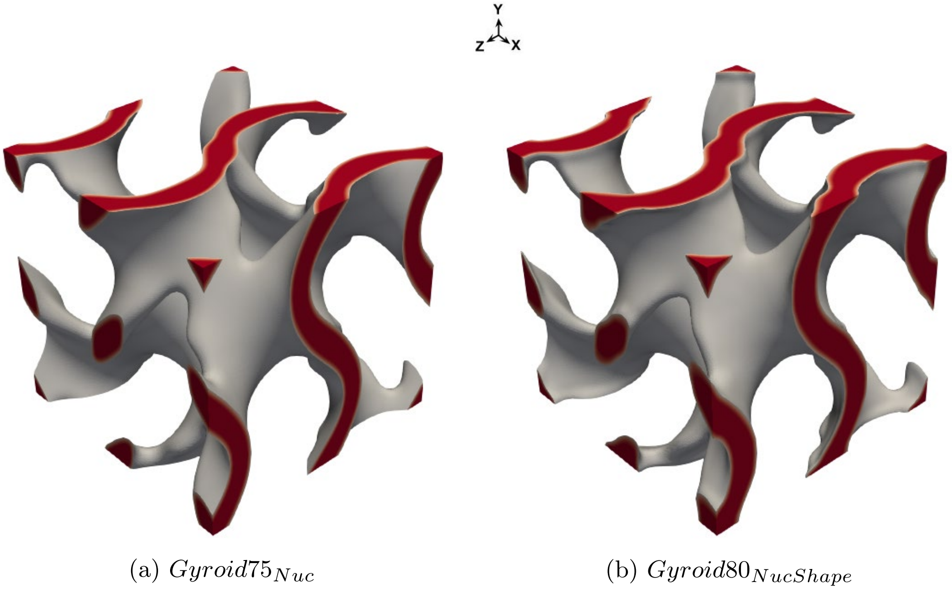

(a) $Gyroid75_{Nuc}$ (b) $Gyroid80_{NucShape}$

Fig. 3 Representation of the modified structures with initial porosities of **a** 75% and **b** 80%

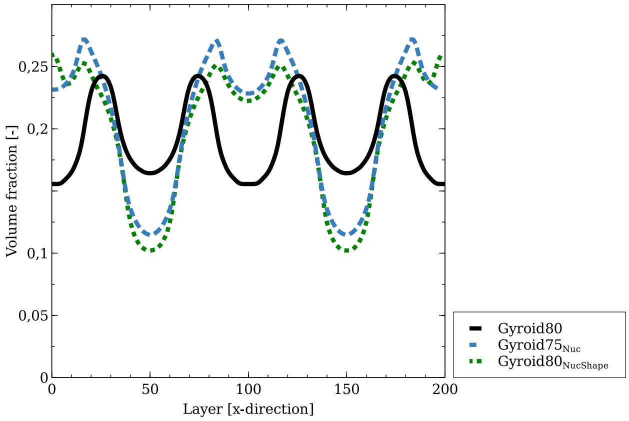

Fig. 4 Volume redistribution of the structure-modified *Gyroid75*$_{Nuc}$ and *Gyroid*80$_{NucShape}$ compared to the gyroid unit cell (black solid line)

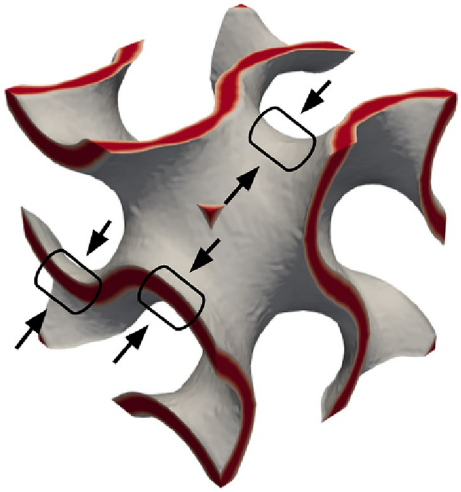

Fig. 5 Highlighted areas of a gyroid structure with 80% porosity where material was removed during the topology modification process

Table 1 Representation of the surface area and volume fraction of the respective structures

	Gyroid80	*Gyroid75*$_{Nuc}$	*Gyroid80*$_{NucShape}$
Volume fraction	0.192	0.207	0.197
Surface area	6.193	5.151	5.101

Despite the similarities in the volume distribution of both structures, slight differences in characteristic features are identified.

As shown in Table 1, the structures exhibit a volume fraction of approximately 20%, corresponding to a porosity of around 80%. This consistent porosity allows for a better comparison between the structures.

In the comparative analysis of surface areas, it becomes evident that the initial gyroid unit cell exhibits the largest surface area, followed by the modified structure *Gyroid75*$_{Nuc}$. This indicates that the phase-field based, load-specific optimization leads to a reduction in surface area.

Despite these differences in surface reduction, a similar increase in the effective elastic modulus in the corresponding loading direction (E_{yy}) is achieved, as shown in Table 2. For independent and improved comparability, the simulation results are presented in a non-dimensionalized form. The modulus of elasticity is given in dimensionless form by E/E_s. In Table 2, the modulus of elasticity in the main load direction is marked in bold. This highlights the efficiency of phase-field based optimization in enhancing mechanical properties, particularly the elastic modulus, even across different topological structures.

By topologically modifying the gyroid unit cell with an original porosity of 75% (*Gyroid75*$_{Nuc}$), an increase in the effective modulus of elasticity in the load direction (E_{yy}) of about 35% is achieved compared to the unmodified gyroid unit cell of the same porosity. For the structure *Gyroid80*$_{NucShape}$, which initially undergoes a volume reduction of 5% due to the

Table 2 Comparison of the non-dimensionalized effective modulus of elasticity in the $x-$, $y-$ and $z-$ directions

	Gyroid80	$Gyroid75_{Nuc}$	$Gyroid80_{NucShape}$
E_{xx}/E_s	0.067	0.023	0.022
E_{yy}/E_s	**0.067**	**0.091**	**0.089**
E_{zz}/E_s	0.067	0.022	0.020

nucleation process and then a further volume increase of 5% due to the shape optimization, the increase in the effective modulus of elasticity of 32% is in a similar range to the structure $Gyroid80_{NucShape}$.

However, it is observed that the optimisation process in the non-loaded directions results in a significant reduction in the effective modulus of elasticity, which is more than half of the original value. This reduction is due to the previously described reduction of the transverse beams in the non-loaded directions, which leads to a pronounced anisotropic behaviour of the cell. In comparison, the original gyroidal unit cell exhibits almost isotropic behaviour, with the effective modulus of elasticity being in a similar range in all load directions.

The next step is to validate the simulatively generated structures and data experimentally.

2.2 Experimental validation

For the experimental validation of the topologically modified unit cells described above, they are multiplied four times in the respective spatial directions and printed out. The unmodified gyroid structure with a porosity of 80% is used as the reference structure. As a result, all three structures have a volume fraction of approximate 20%.

The production of the samples and their subsequent testing are based on the ASTM D1621 standard “Standard Test Method for Compressive Properties Of Rigid Cellular Plastics” [38].

2.2.1 Structure manufacturing

The previously considered unit cells are multiplied 4 times in each spatial direction for the experimental validation, so that the test specimens have a required minimum side length of 25.4mm.

For each sample type, 5 samples are printed using the steriolithography (SL) process. The SL printer from Elegoo Mars 2 and the white standard photopolymer from Elegoo are used for this purpose.

In Fig. 6, one sample type is shown as a representative of the other samples.

Similar to the topology-modified unit cells shown, the difference between the multiplied and printed $Gyroid75_{Nuc}$ and $Gyroid80_{NucShape}$ is barely recognizable. The planar $xy-$direction shows the previously described reduction of the crossbars due to the modification process.

The weight of the respective test specimens, their average weight and the theoretically calculated weight $\bar{g}$ with the volume fractions determined from Table 1 are listed in Table 3.

The table shows that the test specimens exhibit slight weight fluctuations. When comparing the average values (Av) with the theoretically calculated weight values ($\bar{g}$), it becomes clear that they are in a similar range.

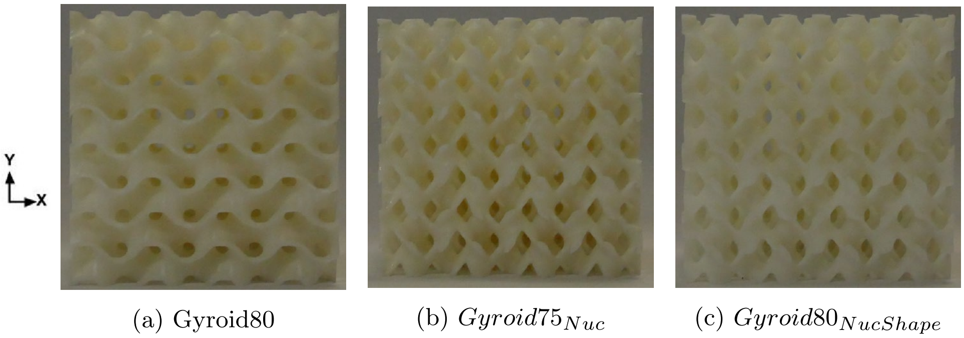

(a) Gyroid80 (b) $Gyroid75_{Nuc}$ (c) $Gyroid80_{NucShape}$

Fig. 6 Planar representation of **a** the unmodified gyroid structure of porosity 80%, the modified structures with the initial porosity of **b** 75% and **c** 80%

Table 3 Weight of the printed samples, their average value (Av) and the theoretically calculated weight value $\bar{g}$

	S1	S2	S3	S4	S5	Av	$\bar{g}$
Gyroid80	31.312	31.616	32.019	31.771	30.836	31.5108	31.09
$Gyroid75_{Nuc}$	33.201	33.299	32.515	33.384	33.074	33.0946	33.52
$Gyroid80_{NucShape}$	30.869	31.847	31.915	31.807	31.994	31.6864	31.90

2.2.2 Mechanical testing condition

The *Inspekt 200* machine from *Hegewald & Peschke* is used to carry out the compression tests for the experimental validation of the unidirectional topology-modified gyroid structures and their reference structure. The initial pressure load starts at 0.03kPa and is applied at a test rate of 2.95mm/min. When about 13% of the original thickness is reached, which corresponds to a distance of about 6.60mm, the test is terminated. For standardized data evaluation, the values are zeroed from a force load of 10N. For the compression tests, the respective test specimens were centrally positioned on the machine's compression plates, as illustrated in Fig. 7 within the red-marked area. Since the specimens exhibit brittle behavior and tend to fracture in multiple directions, a plexiglass shield was placed in front of the machine as a safety precaution.

The calculation of the effective modulus of elasticity (E) from the experimental data is also based on the ASTM D1621 standard, which is calculated as follows:

$$E = \frac{WH}{AD}, \tag{9}$$

where W[N] is the load, H[m] is the height of the undeformed sample, and D[m] is the deformation. $A[\mathrm{m}^2]$ denotes the horizontal cross-sectional area. Since the samples are porous, the horizontal cross-sectional area in $A[\mathrm{m}^2]$, i.e. the area of the samples, is treated as if it were a solid material. The points D and W indicate two points from the linear-elastic range. Since the guideline does not provide specific details on the selection of the points, the local area of each sample is selected where the strain is 0.1%. To determine the value W, the point at 30% of the maximum stress is selected.

2.2.3 Experimental result

The load–displacement curves of the five different samples per specimen type resulting from the compression tests are shown side by side in Fig. 8.

Each sample type is represented by one line type: *Gyroid*80*NucShape* (black solid line), *Gyroid*75*Nuc* (blue dashed line) and *Gyroid*80*NucShape* (green dotted line) structure. For better comparability, the curves of the individual samples are overlaid. It can be seen from the diagrams that the comparative structure (black solid line) shows the smallest increase in the linear elastic range compared to the optimized structures, which is reflected accordingly in the effective modulus of elasticity. It is also recognizable that the maximum load is also lower on average. However, the curve after the load peak

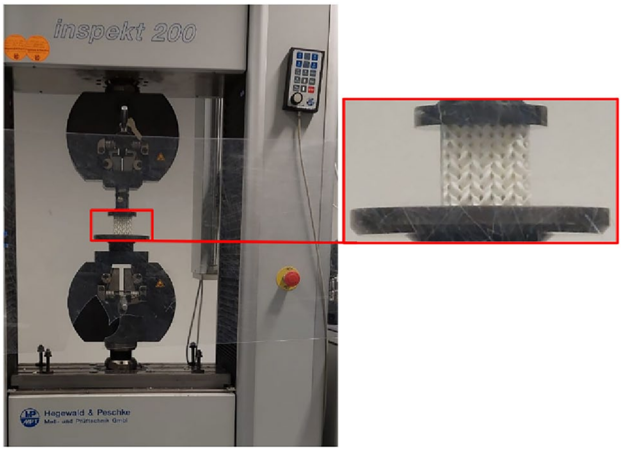

Fig. 7 Testing of the structures: Central positioning of the structures on the compression plate

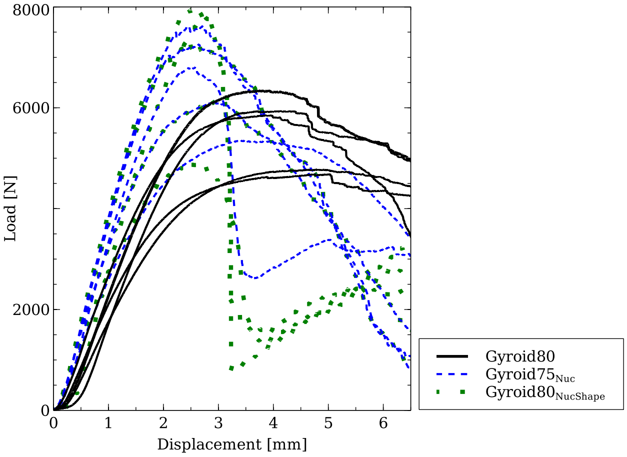

Fig. 8 Load–displacement curves for the five tested samples of the unmodified gyroid structure with a porosity of 80% (black solid line) compared to the modified structures with the initial porosity of 75% (blue dashed line) and 80% (green dotted line)

is flat and more controlled. For the structure *Gyroid75Nuc*, on the other hand, the topology change leads to a rapid drop in some cases. This rapid drop can only be observed in one sample of the structure *Gyroid80NucShape*. From this observation it can be assumed that the subsequent shape optimisation after the topology modification leads to a more uniform failure in the plastic range. For applications where energy absorption plays an important role, this finding is significant.

Table 4 presents the mean value of the effective E-moduli ($\bar{E}$) of the tested samples calculated according to Equation 9 and standard deviation (σ). The value of the individual five samples (E1 to E5) tested can be found in the Table 5 in the appendix.

The increase in the load–displacement curves of the modified structures (Fig. 8), compared to the unmodified gyroid structure, already indicates a higher average modulus of elasticity ($\bar{E}$). This is further confirmed by the calculation of the effective modulus of elasticity in Table 4, where the average modulus for the modified gyroid structures is approximately 20MPa higher than that of the unmodified structure. Additionally, the two modified structures exhibit similar modulus values, but the table also reveals that the modified structures have higher standard deviation. The reasons for the increased standard deviation of the samples must be further validated in future investigations.

The following chapter compares the experimental and simulative data.

2.3 Experimental and simulative comparison

The previous simulative (E_{yy} in Table 2) and experimental ($\bar{E}$ in Table 4) investigations of the effective modulus of elasticity show that a phase-field based topology change and optimization in the linear-elastic range leads to an increase in the effective modulus of elasticity. Consequently, the moduli of elasticity for the structures $Gyroid75_{Nuc}$ and $Gyroid80_{NucShape}$ are, on average, higher than that of the reference structure *Gyroid80*. Furthermore, the experimental results also confirmed the previous simulation observation that the effective modulus of elasticity of the structure $Gyroid75_{Nuc}$ is, on average, slightly higher compared to $Gyroid80_{NucShape}$.

To facilitate a better comparison between the experimentally and numerically determined effective moduli of elasticity, the data for each sample type are presented in a boxplot Fig. 9. In the boxplot, the cross marks the mean value, and the round dots indicate the outliers of the respective sample series. Additionally, the whiskers represent the standard deviation. The red bar indicates the dimensionally simulated modulus of elasticity.

Accordingly, the dimensionalized moduli of elasticity from the simulation (red bar) and the experimental data are in a similar range. However, it should be noted that the lowest scatter is observed in the comparative structure, as can also be seen from the standard deviation (σ) in Table 4. Consequently, no outliers are present in the box plot in Fig. 9a.

Table 4 Calculated mean value of the effective moduli of elasticity ($\bar{E}$) and standard deviation (σ) of the specimes

	Gyroid80 [MPa]	$Gyroid75_{Nuc}$ [MPa]	$Gyroid80_{NucShape}$ [MPa]
$\bar{E}$	47.950	67.695	66.809
σ	6.929	9.673	12.937

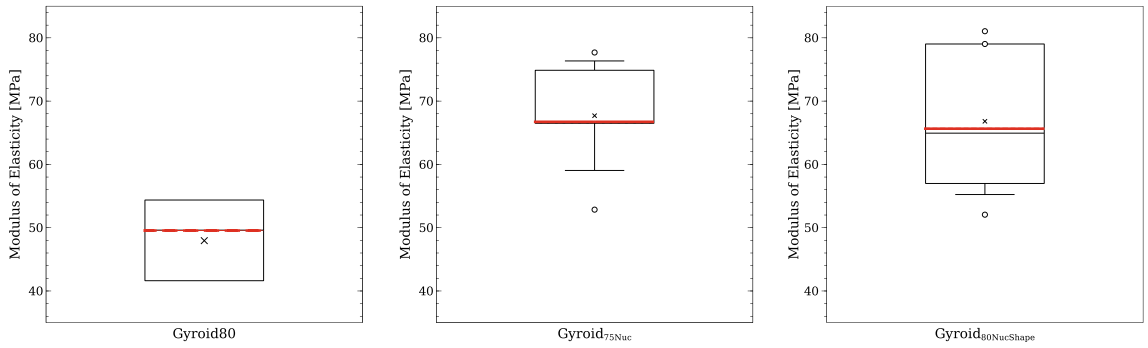

(a) Gyroid80 (b) $Gyroid75_{Nuc}$ (c) $Gyroid80_{NucShape}$

Fig. 9 Comparison of the simulatively (red bar) and experimentally (box plot) determined effective moduli of elasticity of **a** unmodified gyroid structure with a porosity of 80%, the modified structures with the initial porosity of **b** 75% and **c** 80%

Table 5 Calculated effective modulus of elasticity of the specimes

	Gyroid80 [MPa]	$Gyroid75_{Nuc}$ [MPa]	$Gyroid80_{NucShape}$ [MPa]
E1	49.612	66.485	56.986
E2	39.777	52.850	79.024
E3	54.370	74.870	81.043
E4	54.370	77.683	52.054
E5	41.620	66.584	64.935

Additionally, the determined data range for *Gyroid80* aligns with the simulated effective modulus of elasticity calculated by another study [26] for the gyroid structure with a porosity of 80%.

Overall, it is demonstrated that optimization in the linear elastic range results in noticeable changes in both, the linear elastic and plastic ranges. A pure topology change leads to an increase in the modulus of elasticity, which has been confirmed both numerically and experimentally.

3 Conclusion

In this study, two gyroid structures with a final porosity of 80%, were topology-modified and topolgy-shape-modified by simulations based on the phase-field method. Results of the effective modulus of elasticity compare well with the experimental measurements. An unmodified gyroid structure with a porosity of 80% also served as a comparative structure.

In the first method, a gyroid structure with an initial porosity of 75% was reduced by approx. 5% through targeted volume reduction. In the second method, the gyroid structure has an initial porosity of 80%, after a volume reduction of also approx.5%, a phase-field based shape optimization was then carried out until the initial porosity of 80% was reached.

It could be shown both simulatively and experimentally that the structural modification in both variants leads to an increase in the effective modulus by 32%.

The experimental validation confirmed that the optimization in the linear elastic range led on average to an increase in the maximum load, and it was observed that the structures exhibited a change in the plastic range. While the only topologically modified structures predominantly exhibited a rapid drop in the load–displacement curve, the curves in the plastic range were flatter in the specimens with subsequent shape optimization. However, this observation that subsequent shape optimization leads to a flattened displacement curve in the plastic range still needs to be validated experimentally in further studies. This observation would be important for applications in which the energy absorption capacity is the center of attention.

Overall, the phase field method has proven to be a promising optimization method for complex porous three-dimensional structures. The study highlights the significant impact of topology modification and optimization on the mechanical properties of gyroid structures. The observed increase in the modulus of elasticity due the structural modifications proposed by phase-field modelling underscores the potential of this approach for developing advanced materials with tailored properties. Furthermore, phase-field based shape and topology optimization can be extended to other cellular structures, enabling load-specific design optimizations for a diverse range of applications, from heat exchangers in aerospace to crash-resistant structures in civil engineering. The phase field method offers more intensive investigation and expansion options for optimization. As a future research perspective, the phase-field based optimization process can be adapted to additive manufacturing processes.

Acknowledgements Thanks go to Dr. Martin Reder for his spontaneous proofreading. Also to Ines Kirchlechner and Nils Kersch, who were involved in the manufacture and testing of the samples, and also to the Federal Ministry of Economics and Climate Protection for their funding of the ZIM projects KK5134113SK1 and KK5446701SK1. Additionally, we would like to express our gratitude to the programme "Mittelbau" funded by the ministry of Science, Research and Arts Baden-Württemberg. Furthermore, contributions with respect to model development and programming have been made through the financial support of the Helmholtz association within the programme "MSE" no. 43.31.01, which is gratefully acknowledged. This work was performed on the computational resource bwUniCluster funded by the Ministry of Science, Research and the Arts Baden-Württemberg and the Universities of the State of Baden-Württemberg, Germany, within the framework program bwHPC.

Author Contributions LW wrote the main manuscript text. MS1, FP, and BN are supervisors. MS2 is a project member.

Funding Open Access funding enabled and organized by Projekt DEAL. This research received funding from Helmholtz Association, "MSE" no. 43.31.01, Federal Ministry of Economics and Climate Protection (KK5134113SK1, KK5446701SK1), and Ministry of Science, Research and Arts Baden-Württemberg (programme "Mittelbau").

Data Availability The data that support the findings of this study are available from the corresponding author upon reasonable request.

Declarations

Ethics approval and consent to participate This article does not contain any studies with human participants or animals performed by any of the authors.

Competing interests The authors do not have any Conflict of interest.

Appendix

References

1. Yang S, Deng S, Kuang H, Zhou D, Gong X, Dong K. Evaluating and comparing the natural cell structure and dimensions of honey bee comb cells of Chinese Bee, Apis cerana cerana (Hymenoptera: Apidae) and Italian Bee, Apis mellifera ligustica (Hymenoptera: Apidae). J Insect Sci. 2021;21(4):1.
2. Li T, Sun J, Leng J, Liu Y. In-plane mechanical properties of a novel cellular structure for morphing applications. Compos Struct. 2023;305:116482. https://doi.org/10.1016/j.compstruct.2022.116482.
3. Pan C, Han Y, Lu J. Design and optimization of lattice structures: a review. Appl Sci. 2020;10(18):6374. https://doi.org/10.3390/app10186374.
4. Bari K, Bollenbach L. Spiderweb cellular structures manufactured via additive layer manufacturing for aerospace application. J Compos Sci. 2022;6(5):133. https://doi.org/10.3390/jcs6050133.
5. Tian L, Sun B, Yan X, Sharf A, Tu C, Lu L. Continuous transitions of triply periodic minimal surfaces. Addit Manuf. 2024;84:104105. https://doi.org/10.1016/j.addma.2024.104105.
6. Maskery I, Aboulkhair NT, Aremu AO, Tuck CJ, Ashcroft IA. Compressive failure modes and energy absorption in additively manufactured double gyroid lattices. Addit Manuf. 2017;16:24–9. https://doi.org/10.1016/j.addma.2017.04.003.
7. Chenxi Peng PM, Tran P. Triply periodic minimal surfaces based honeycomb structures with tuneable mechanical responses. Virtual Phys Prototyp. 2023;18(1):2125879. https://doi.org/10.1080/17452759.2022.2125879.

8. Maevskaia E, Guerrero J, Ghayor C, Bhattacharya I, Weber F. Tpms-based scaffolds for bone tissue engineering: a mechanical, in vitro and in vivo study. Tissue Eng Part A. 2023;29(19–20):507–17. https://doi.org/10.1089/ten.TEA.2023.0033.
9. Ma W, Li Z, Xie S. Crashworthiness analysis of thin-walled bio-inspired multi-cell corrugated tubes under quasi-static axial loading. Eng Struct. 2020;204:110069. https://doi.org/10.1016/j.engstruct.2019.110069.
10. Collins M, Ren G, Young K, Pina S, Reis R, Oliveira J. Scaffold fabrication technologies and structure/function properties in bone tissue engineering. Adv Funct Mater. 2021;31(21):2010609. https://doi.org/10.1002/adfm.202010609.
11. Zhang L, Song B, Choi S-K, Shi Y. A topology strategy to reduce stress shielding of additively manufactured porous metallic biomaterials. Int J Mech Sci. 2021;197:106331. https://doi.org/10.1016/j.ijmecsci.2021.106331.
12. Wallat L, Koeppe A, Selzer M, Seiler M, Poehler F, Nestler B. Experimental evaluation of phase-field-based load-specific shape optimization of nature-inspired porous structures. Mater Today Commun. 2024;38:108088. https://doi.org/10.1016/j.mtcomm.2024.108088.
13. Al-Ketan O, Rowshan R, Abu Al-Rub RK. Topology-mechanical property relationship of 3d printed strut, skeletal, and sheet based periodic metallic cellular materials. Addit Manuf. 2018;19:167–83. https://doi.org/10.1016/j.addma.2017.12.006.
14. Wakjira Y, Cioni A, Lemu H. Current status of the application of additive-manufactured TPMS structure in bone tissue engineering. Prog Addit Manuf. 2024;10:1085–102. https://doi.org/10.1007/s40964-024-00714-w.
15. Wang J, Qian C, Qiu X, Yu B, Yan L, Shi J, Chen J. Numerical and experimental investigation of additive manufactured heat exchanger using triply periodic minimal surfaces (tpms). Therm Sci Eng Prog. 2024;55:103007. https://doi.org/10.1016/j.tsep.2024.103007.
16. Schumacher A. Optimierung Mechanischer Strukturen: Grundlagen und Industrielle Anwendungen. 2020. https://doi.org/10.1007/978-3-662-60328-4.
17. Wallat L, Altschuh P, Reder M, Nestler B, Poehler F. Computational design and characterisation of gyroid structures with different gradient functions for porosity adjustment. Materials. 2022;15(10):3730. https://doi.org/10.3390/ma15103730.
18. Dong Z, Zhao X. Application of TPMS structure in bone regeneration. Eng Regen. 2021;2:154–62. https://doi.org/10.1016/j.engreg.2021.09.004.
19. Gao S, Qu S, Ding J, Liu H, Song X. Influence of cell size and its gradient on thermo-hydraulic characteristics of triply periodic minimal surface heat exchangers. Appl Therm Eng. 2023;232:121098. https://doi.org/10.1016/j.applthermaleng.2023.121098.
20. Bendsøe MP. Optimization of structural topology, shape, and material, vol. 414. Berlin; Heidelberg: Springer; 1995.
21. Strömberg N. A two-variable topology optimization approach for simultaneously macro layout and local grading of periodic lattice structures. 2020.
22. Günther F, Pilz S, Hirsch F, Wagner M, Kästner M, Gebert A, Zimmermann M. Shape optimization of additively manufactured lattices based on triply periodic minimal surfaces. Addit Manuf. 2023;73:103659. https://doi.org/10.1016/j.addma.2023.103659.
23. Li X, Lowengrub J, Rätz A, Voigt A. Solving PDES in complex geometries: a diffuse domain approach. Commun Math Sci. 2009;7(1):81–107. https://doi.org/10.4310/cms.2009.v7.n1.a4.
24. Takezawa A, Koizumi Y, Kobashi M. High-stiffness and strength porous maraging steel via topology optimization and selective laser melting. Addit Manuf. 2017;18:194–202. https://doi.org/10.1016/j.addma.2017.10.004.
25. Wallat L, Reder M, Selzer M, Poehler F, Nestler B. Shape optimization of porous structures by phase-field modeling with strain energy density reduction. Mater Today Commun. 2023;37:107018. https://doi.org/10.1016/j.mtcomm.2023.107018.
26. Wallat L, Kersch N, Reder M, Selzer M, Seiler M, Poehler F, Nestler B. Phase-field based shape optimization of uni- and multiaxially loaded nature-inspired porous structures while maintaining characteristic properties. 2024. https://doi.org/10.1007/s44245-024-00065-4.
27. Yu Q, Xia Q, Li Y. A phase field-based systematic multiscale topology optimization method for porous structures design. J Comput Phys. 2022;466:111383. https://doi.org/10.1016/j.jcp.2022.111383.
28. Wallin M, Ristinmaa M. Howard's algorithm in a phase-field topology optimization approach. Int J Numer Method Eng. 2013;94(1):43–59. https://doi.org/10.1002/nme.4434.
29. Xie W, Xia Q, Yu Q, Li Y. An effective phase field method for topology optimization without the curvature effects. Comput Math Appl. 2023;146:200–12. https://doi.org/10.1016/j.camwa.2023.06.037.
30. Hötzer J, Reiter A, Hierl H, Steinmetz P, Selzer M, Nestler B. The parallel multi-physics phase-field framework pace3d. J Comput Sci. 2018;26:1–12. https://doi.org/10.1016/j.jocs.2018.02.011.
31. Allen SM, Cahn JW. A microscopic theory for antiphase boundary motion and its application to antiphase domain coarsening. Acta Metall. 1979;27(6):1085–95. https://doi.org/10.1016/0001-6160(79)90196-2.
32. Garcke H, Nestler B, Stoth B. A multiphase field concept: Numerical simulations of moving phase boundaries and multiple junctions. SIAM J Appl Math. 1999;60(1):295–315. https://doi.org/10.1137/S0036139998334895.
33. Nestler B, Wendler F, Selzer M, Stinner B, Garcke H. Phase-field model for multiphase systems with preserved volume fractions. Phys Rev E. 2008;78:011604. https://doi.org/10.1103/PhysRevE.78.011604.
34. Sun Y, Beckermann C. Sharp interface tracking using the phase-field equation. J Comput Phys. 2007;220(2):626–53. https://doi.org/10.1016/j.jcp.2006.05.025.
35. Schoof E, Schneider D, Streichhan N, Mittnacht T, Selzer M, Nestler B. Multiphase-field modeling of martensitic phase transformation in a dual-phase microstructure. Int J Solids Struct. 2018;134:181–94. https://doi.org/10.1016/j.ijsolstr.2017.10.032.
36. Prahs A, Reder M, Schneider D, Nestler B. Thermomechanically coupled theory in the context of the multiphase-field method. Int J Mech Sci. 2023;257: 108484. https://doi.org/10.1016/j.ijmecsci.2023.108484.
37. Reder M, Holland-Cunz J, Lorson P, August A, Nestler B. Simulative determination of effective mechanical properties for digitally generated foam geometries. Adv Eng Mater. 2023;25(19):2300340. https://doi.org/10.1002/adem.202300340.
38. Standard Test Method for Compressive Properties Of Rigid Cellular Plastics (2000)